Available online at www.sciencedirect.com
ScienceDirect
International Journal of Heat and Mass Transfer 51 (2008) 1516–1529
International Journal of HEAT and MASS TRANSFER
www.elsevier.com/locate/ijhmt

Numerical investigation on the evaporation of droplets depositing on heated surfaces at low Weber numbers

George Strotos [a,1], Manolis Gavaises [b,*], Andreas Theodorakakos [c], George Bergeles [a,1]

[a] Department of Mechanical Engineering, National Technical University of Athens, 5 Heroon Polytechniou, Zografos, 15710 Athens, Greece
[b] School of Engineering and Mathematical Sciences, The City University, Northampton Square, EC1V 0HB London, UK
[c] Fluid Research Company, Laskareos 49, 11472 Athens, Greece

Received 12 February 2007
Available online 1 October 2007

Abstract

The evaporation of water droplets, impinging with low Weber number and gently depositing on heated surfaces of stainless steel is studied numerically using a combination of fluid flow and heat transfer models. The coupled problem of heat transfer between the surrounding air, the droplet and the wall together with the liquid vaporisation from the droplet's free surface is predicted using a modified VOF methodology accounting for phase-change and variable liquid properties. The surface cooling during droplet's evaporation is predicted by solving simultaneously with the fluid flow and heat transfer equations, the heat conduction equation within the solid wall. The droplet's evaporation rate is predicted using a model from the kinetic theory of gases coupled with the Spalding mass transfer model, for different initial contact angles and substrate's temperatures, which have been varied between 20–90° and 60–100 °C, respectively. Additionally, results from a simplified and computationally less demanding simulation methodology, accounting only for the heat transfer and vaporisation processes using a time-dependent but pre-described droplet shape while neglecting fluid flow are compared with those from the full solution. The numerical results are compared against experiments for the droplet volume regression, life time and droplet shape change, showing a good agreement.

Keywords: Droplet; Evaporation; VOF; Heated plate

1. Introduction

Liquid–vapour phase-change processes play a significant role in a number of technological applications in combustion engines, cooling systems and refrigeration cycles. The dynamic behaviour of the impinging droplets together with the heat transfer process between the liquid and the heated surface affect the liquid–vapour phase-change conditions. The mechanism of the droplet spreading and the accompanying heat transfer is governed by well known non-dimensional numbers, namely the Weber (*We*), Reynolds (*Re*), Eckert (*Ec*), Froude (*Fr*) and Bond (*Bo*) numbers as well as the temperature of the surface. As the cooler droplet impacts upon the hotter solid surface, heat is transferred from the solid to the liquid phase. The heat transfer to the droplet increases the mean temperature of the liquid, while vaporisation takes place. The collision dynamics of a liquid droplet impinging on a hot surface has attracted attention in a number of experimental studies; some relevant publications [1–9] refer to a number of experiments performed in this area. Based on the evaporation lifetime of a droplet, mainly four different evaporation regimes can be identified depending on the wall temperature: film evaporation, nucleate boiling, transition boiling and film boiling. One more important parameter affecting wall surface cooling and being essential not only for the

* Corresponding author. Tel.: +44 2070408115; fax: +44 2070408101.
E-mail addresses: m.gavaises@city.ac.uk (M. Gavaises), andreas@fluid-research.com (A. Theodorakakos), bergeles@fluid.mech.ntua.gr (G. Bergeles).
[1] Tel.: +30 2107721058; fax: +30 2107723616.

0017-9310/$ - see front matter © 2007 Elsevier Ltd. All rights reserved.
doi:10.1016/j.ijheatmasstransfer.2007.07.045

Nomenclature

A	surface area (m^2)
B_M	Spalding number
Bo	Bond number, $Bo = \rho_{liq} g L_{ref}^2/\sigma$
C	vapour concentration (full solution) (kg/kg)
c_p	heat capacity (J/kgK)
D	diameter (m)
D_{AB}	vapour diffusion coefficient (m^2/s)
Ec	Eckert number, $Ec = U^2/(c_p \Delta T)$
Fr	Froude number, $Fr = U^2/(gL)$
f_σ	volumetric force due to surface tension (N)
g	gravity (m/s^2)
Gr	Grashof number, $Gr = g \cdot \beta \cdot \Delta T \cdot D^3/v^2$
h_{conv}	heat transfer coefficient (W/(m^2K))
h_m	mass transfer coefficient (m/s)
k	thermal conductivity (W/(mK))
L	latent heat of vaporisation (J/kg)
L_{ref}	reference length (m)
m	mass (kg)
$\dot{m}_{evap}$	evaporation rate (kg/s)
MW	molar weight (kg/kmol)
Nu	Nusselt number, $Nu = h_{conv} L_{ref}/k$
p	pressure (Pa)
Pr	Prandtl number, $Pr = \mu \cdot c_p/k$
$\Re$	universal gas constant (J/(kmol K)
Re	Reynolds number, $Re = u \cdot D/v$
Sh	Sherwood number, $Sh = h_m L_{ref}/D_{AB}$
T	temperature (K)
$\vec{T}$	stress tensor
u	velocity (m/s)
V	droplet volume (m^3)
V_{cell}	cell volume (m^3)
We	Weber number, $We = \rho U^2 D/\sigma$
Y	vapour concentration (simplified model) (kg/kg)

Greek symbols

α	liquid volume fraction in cell, V_{liq}/V_{cell}
ε	cooling effectiveness factor
θ	contact angle (°)
κ	curvature (m^{-1})
λ	thermal accommodation coefficient
μ	viscosity (kg/(ms))
ρ	density (kg/m^3)
σ	surface tension (N/m)

Subscripts

0	initial
cont	contact
conv	convection
drop	droplet
evap	evaporation
gas	gas phase
liq	liquid phase
m	mixture
∞	infinity
s	saturation
sol	solid
surf	surface
vap	vapour

description of physics of this phenomenon but also for its numerical simulation, is the value of contact angle at the air–liquid–solid triple line. In [8,9] the sessile drop technique has been used to measure the variation of contact angles for an aluminium surface, as a function of surface temperature, while in [10] the effect of contact angles on droplet evaporation was studied.

Due to the complexity of these physical processes, development of numerical methods to predict the associated heat and mass transfer is a complicated task. Nevertheless, research efforts over several years have provided an understanding of many aspects of vaporisation or condensation. The MAC-type solution method has been used in [11,12], employing a finite-differencing approximation of the Navier–Stokes equations expressed for axisymmetric and incompressible fluid flows. Fluid motion was induced by a pre-defined temperature distribution between the lower and the upper side of the droplet. The unsteady thermal distribution inside the droplet was not calculated, assuming the temperature of the droplet's bottom to be at the saturation temperature and that a vapour layer exists between the droplet and solid surface. A number of analytical studies [13–17] address the Leidenfrost phenomenon or the steady-state droplet film boiling regime. In [18] a complete numerical solution of the Navier–Stokes and energy equation based on a modified SOLA-VOF method for modelling droplet deformation and solidification, including heat transfer in the substrate was used. The heat transfer coefficient at the droplet–substrate interface was estimated by matching numerical predictions of the variation of substrate temperature with measurements. Heat transfer in the droplet was modelled by solving the energy equation, but viscous dissipation was neglected. Later, the authors of [19] extended the model developed in [20] and combined a fixed-grid control volume discretisation of the flow field and energy equations with a volume tracking algorithm to track the droplet free surface. Surface tension effects were also taken into account. The energy equation in both the liquid and the solid portion of the droplet were solved using the enthalpy equation in the case of solidification. More recent three-dimensional CFD codes have been used to model complex flows such as impact on inclined surfaces in [21] and droplet break-up in [22]. In [21] an adaptive level-set method for moving boundary problems in the case of droplet spreading and solidification was developed. In [23,24] the fluid dynamics and heat transfer phenomena

were studied numerically both inside a droplet and the substrate based on a Lagrangian formulation and utilising the finite element method using a deforming mesh. The temperature field developing in both the liquid droplet and the substrate during the impingement process was also determined. The authors of [25] followed the Lagrangian formulation including surface tension and heat transfer. They investigated the effect of initial droplet temperature, impact velocity, thermal contact resistance and initial substrate temperature on droplet spreading, final deposit shapes and time to initiate and complete freezing. In [26] the energy equation was solved in both the droplet and substrate domain, implementing a time and space averaged thermal contact resistance between the two materials. During calculations, a technique for mesh regeneration was used in order to enhance accuracy. In [27–29] a VOF methodology was presented, coupling an one-dimensional algorithm for modelling the hydrodynamic gross deformation of the droplet impacting onto a hot wall surface and the fluid flow within the viscous vapour layer existing between the droplet and the solid surface. The height of the vapour layer was assumed to be several orders of magnitude smaller than the dimensions of the droplet, resulting in a Knudsen number approaching values of the order of 0.1 during droplet impact simulations. It is important to note that the height of the vapour layer was not a result of the solution of the Navier–Stokes equations, but it was assumed to be known. Furthermore, a kinetic theory-based treatment was employed for calculating the conditions on the non-equilibrium interfaces of the vapour layer by solving the heat transfer rate within the solid, the liquid and the vapour phases. This model was validated for a number of droplet impact conditions including a wide range of *We* number impacts and initial droplet and surface temperature. In [30] a model applicable to droplets evaporating on a high thermal conductivity surface is proposed; in this model it has been assumed that the solid surface temperature is constant during droplet evaporation, the contact angle decreases continuously during droplet evaporation and the diameter of the wetted region under the droplet remains constant. In contrast, the authors of [31] assumed constant contact angle during the entire evaporation process, which can only be an accurate approximation during the last stage of droplet evaporation when the receding contact angle has been reached. This is addressed in [10] where a model has been proposed for predicting the evaporation of a droplet in contact with a heated wall and the cooling of the solid plate; based on experimental observations, it has been assumed that the deposited droplet is a spherical cap and the contact angle is decreasing continuously during droplet evaporation, while the diameter of the wetted area under the droplet remains constant. Once the limit of the receding angle is reached, the liquid–solid contact angle remains constant, but the contact diameter decreases following the liquid volume reduction, as in [31]. In [32] a constant surface temperature has been assumed for a high thermal conductivity aluminium substrate while the internal liquid motion has been taken into consideration. The results have been compared with a model accounting only for the heat conduction and revealing great differences between the two approaches.

From the above discussion becomes clear that so far no study has actually taken into account consistently all the effects taking place during the vaporisation of a droplet deposited on a heated plate. This is addressed in the present study where the coupled fluid flow and heat transfer equations are simultaneously solved both for the liquid and the solid by considering the local vaporisation rate at the liquid–air interface and accounting for variable physical properties as function of local temperature. Predictions are performed and compared with the experiments of [10,33], which address the effects of the initial contact angle and solid surface temperature on droplet evaporation. Past work from the authors' group presented in [34,35] thoroughly describes the numerical tools used to predict the different flow regimes formed during impaction of droplets on liquid surfaces. Here emphasis is given to the description of the vaporisation models themselves. This represents an extension of the model used in [35] and in which the vaporisation rate model was based on the well known Sherwood number correlations for heat/mass transfer of spherical droplets. To avoid this restriction, a local vaporisation rate model is derived here independently of the droplet shape. This model is validated against predictions of the well known correlations of the integral vaporisation rate of spherical droplets. In addition to the full fluid flow and heat transfer equations, a simplified model, initially proposed by Chandra et al. [10], is also used here for comparing the results of the full solution with previously presented simpler and less demanding computational models. From this comparison, the effect on the vaporisation rate of the liquid flow motion is quantified.

In the next section of the paper, a description of the test cases simulated is presented, followed by description of the mathematical model and the obtained results. The most important conclusions are summarised at the end.

2. Test cases simulated

According to data reported in [10,33] water droplets fall from a height of 50 mm onto a hot stainless steel surface. The impact velocity is approximately 1.0 m/s and the Weber number varied from 27 to 41 for all cases tested, which is small enough to result to droplet deposition on the solid surface. The plate thickness is 6.35 mm and its surface area is 50.8×50.8 mm^2; the plate is heated from below by two 125 W heaters while its temperature was measured by a thermocouple. The initial liquid–solid contact angle was controlled by adding a surfactant (sodium dodecyl sulfate) in water. The surfactant concentrations used were 0 ppm, 100 ppm and 1000 ppm by weight, which result to 90°, 55° and 20° equilibrium contact angles, respectively. These concentrations are low enough to leave the thermophysical properties of water unaffected. The droplet sizes for

the three different surfactant concentration levels were 2.05 mm, 2.02 mm and 2.07 mm, respectively. The initial surface temperature was set between 60 °C and 100 °C, which is low enough for nucleate boiling regime to prevail. The ambient room temperature of 20 °C and atmospheric pressure were held constant during the experiment, while the initial droplet temperature was 20 °C. Droplet evaporation was recorded using a high resolution video camera. The droplet volume was determined by measuring the liquid/solid contact diameter and the droplet height, and assuming the droplet to be a spherical cap section.

3. Simulation model

Simulation of the above described experiment is performed by dividing the relevant fluid and heat transfer processes into two stages. In the first stage, the droplet dynamics from the time it impacts onto the wall until it reaches an equilibrium state is investigated. During this transitional period the droplet's mean temperature and vaporisation process are estimated. These calculations show that freezing of the droplet surface translational motion is achieved at approximately within 1% of the total droplet vaporisation time. In the second stage, which lasts for the 99% of the total droplet life time, the evaporation of the droplet is studied effectively without droplet transitional motion and with fluid circulation induced by the heat transfer process. This stage is examined using two different approaches. Initially, the full set of Navier–Stokes equations including energy and vapour transport equation coupled with VOF methodology, are solved simultaneously with the heat conduction equation inside the solid wall. Alternatively, a simplified model is used in order to reduce the calculation time. In this model only the evaporation and heat conduction processes between the liquid and the wall are considered while the droplet shape is pre-defined up to complete liquid vaporisation, as described above in [10].

3.1. VOF methodology

The flow induced by the impact of a droplet on a hot surface is considered as two-dimensional and axisymmetric. For identifying each phase separately a volume fraction, denoted by α, is introduced following the volume of fluid method (VOF), initially proposed in [36]. In the VOF method the volume fraction α is defined as

$$\alpha = \frac{\text{Volume of liquid phase}}{\text{Total volume of the control volume}} \tag{1}$$

where the α-function is 1 inside the liquid, 0 in the gas phase and values between 0 and 1 in the interface area. The transport equation of the volume fraction α, taking into account the effects of evaporation and liquid thermal expansion is given by

$$\frac{\partial a}{\partial t} + \nabla(au) = -\frac{1}{\rho_{\text{liq}}}\frac{\dot{m}_{\text{evap}}}{V_{\text{cell}}} - \alpha\frac{1}{\rho_{\text{liq}}}\frac{\mathrm{D}\rho_{\text{liq}}}{\mathrm{D}t} \tag{2}$$

The momentum equations expressing both phases are written in the form

$$\frac{\partial(\rho\vec{u})}{\partial t} + \nabla\cdot(\rho\vec{u}\otimes\vec{u} - \vec{T}) = \rho\vec{g} + \vec{f}_{\sigma} \tag{3}$$

where $\vec{T}$ is the stress tensor, $\vec{u}$ is the velocity and f_σ is the volumetric force due to surface tension. The value of f_σ is equal to $f_\sigma = \sigma\cdot\kappa\cdot(\nabla a)$, where σ is the numerical value of the surface tension and κ is the curvature of the interface region. The flow field is solved numerically on two unstructured grids, using a recently developed adaptive local grid refinement technique in order to track the liquid–gas interface. A detailed discussion of the fluid flow model used here is presented in [35], while the adaptive local grid refinement technique used in order to enhance accuracy of the predictions in the areas of interest (i.e. the liquid–gas interface), with the minimum computational cost can be found in [37]. To account for the high flow gradients near the free surface, the cells are locally subdivided to various resolution levels, prescribed by the user in either sides of the free surface. As a result, the interface is always enclosed by the densest grid region. A new locally refined mesh is created every 20 time steps. Fig. 1 shows a typical example of the application of the local refinement technique to the case studied here.

The high resolution differencing scheme CICSAM, proposed in [38] in the transport equation for the volume fraction α is used. The discretisation of the convection terms of the velocity components is based on a high resolution convection–diffusion differencing scheme proposed in [39]. The time derivative was discretised using a second-order differencing scheme (Crank–Nicolson). Finally, the contact angles at the advancing and receding contact lines are assigned as boundary conditions. Additionally the energy transport equation and the vapour transport equation are solved

$$\rho c_{\text{p}}\frac{\mathrm{D}T}{\mathrm{D}t} = \nabla(k\nabla T) + \frac{\mathrm{D}p}{\mathrm{D}t} - \frac{\dot{m}_{\text{evap}}L}{V_{\text{cell}}} \tag{4}$$

$$(1-\alpha)\rho_{\text{gas}}\frac{\mathrm{D}C}{\mathrm{D}t} = \nabla[(1-\alpha)\rho_{\text{gas}}D_{\text{AB}}\nabla C] + \frac{\dot{m}_{\text{evap}}}{V_{\text{cell}}} \tag{5}$$

For the mixed phase of liquid and gas, while gas phase is a mixture of air and vapour phase, most of the physical and thermodynamic properties are calculated as a function of volume fraction α, using linear interpolation between the values of the two phases

$$\begin{aligned}\rho &= \alpha\rho_{\text{liq}} + (1-\alpha)\rho_{\text{gas}}\\ \mu &= \alpha\mu_{\text{liq}} + (1-\alpha)\mu_{\text{gas}}\\ Pr &= \alpha Pr_{\text{liq}} + (1-\alpha)Pr_{\text{gas}}\end{aligned} \tag{6}$$

Heat capacity is calculated as mass and not volume weighted for a computational cell, i.e.

$$c_{\text{p}} = \frac{m_{\text{liq}}}{m_{\text{tot}}}\cdot c_{\text{p,liq}} + \left(1 - \frac{m_{\text{liq}}}{m_{\text{tot}}}\right)\cdot c_{\text{p,gas}} \tag{7}$$

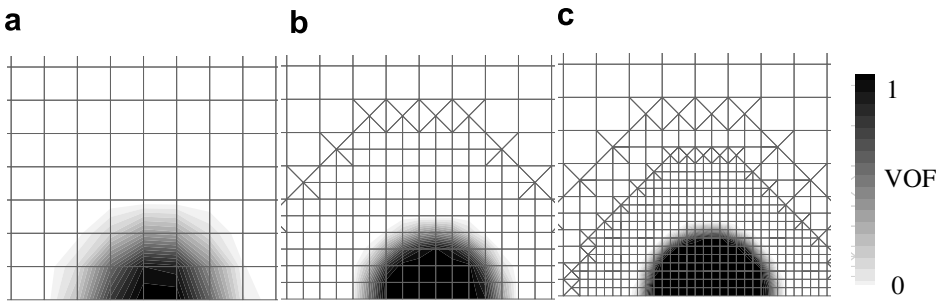

Fig. 1. Numerical grids showing successive grid refinements for better representation of the liquid–gas interface (a) without grid refinement, (b) one-level of grid refinement and (c) two-levels of grid refinement. Grid is automatically refined as the liquid surface moves.

and the masses are calculated as

$$m_{\text{tot}} = \rho \cdot V_{\text{cell}}$$
$$m_{\text{liq}} = \alpha \cdot \rho_{\text{liq}} \cdot V_{\text{cell}} \tag{8}$$

The properties of gas mixture are calculated as a function of vapour concentration C, using linear interpolation between the values of the thermodynamic properties of pure air and vapour

$$\mu_{\text{gas}} = C \cdot \mu_{\text{vap}} + (1 - C) \cdot \mu_{\text{air}}$$
$$c_{\text{p,gas}} = C \cdot c_{\text{p,vap}} + (1 - C) \cdot c_{\text{p,air}}$$
$$Pr_{\text{gas}} = C \cdot Pr_{\text{vap}} + (1 - C) \cdot Pr_{\text{air}}$$
$$\rho_{\text{gas}} = \frac{p}{\Re / MW_{\text{gas}} \cdot T}, \quad MW_{\text{gas}} = \left(\frac{C}{MW_{\text{vap}}} + \frac{1 - C}{MW_{\text{air}}} \right)^{-1} \tag{9}$$

The properties of the pure species (liquid, air and vapour) are assumed to be function of temperature [40] and thus they are updated at every calculation time step.

3.2. VOF evaporation model

An important part of the simulation is the modelling of evaporation source terms. The model used is based on Fick's law using as driving force the local concentration gradient in the interface and assuming that the interface is saturated. The evaporation rate is given by

$$\dot{m}_{\text{evap}} = \frac{\mathrm{d}m}{\mathrm{d}t} = \rho_{\text{gas}} D_{\text{AB}} A_{\text{liq-cell}} \left(\frac{\mathrm{d}C}{\mathrm{d}n} \right)_{\text{surf}}$$
$$A_{\text{liq-cell}} = V_{\text{cell}} |\nabla a| \tag{10}$$

This model is independent of the flow conditions and shape of the liquid–air interface. In order to validate the evaporation model, a test case of a single droplet was considered. A standing liquid droplet of n-nonane with an initial uniform temperature of 300 K was left to vaporise in an environment of 400 K temperature under atmospheric pressure. As reference, the Spalding's infinite conductivity model was employed, which assumes uniform temperature inside the droplet, and thus it is referred to as 0-D model

$$\dot{m}_{\text{evap}} = \frac{\mathrm{d}m}{\mathrm{d}t} = h_{\text{m}} \rho_{\text{gas}} A_{\text{drop}} \cdot \ln(1 + B_M)$$
$$h_{\text{m}} = \frac{Sh \cdot D_{\text{AB}}}{L_{\text{ref}}}, \quad Sh = 2$$
$$B_M = \frac{Y_{\text{s}} - Y_{\infty}}{1 - Y_{\text{s}}} \tag{11}$$

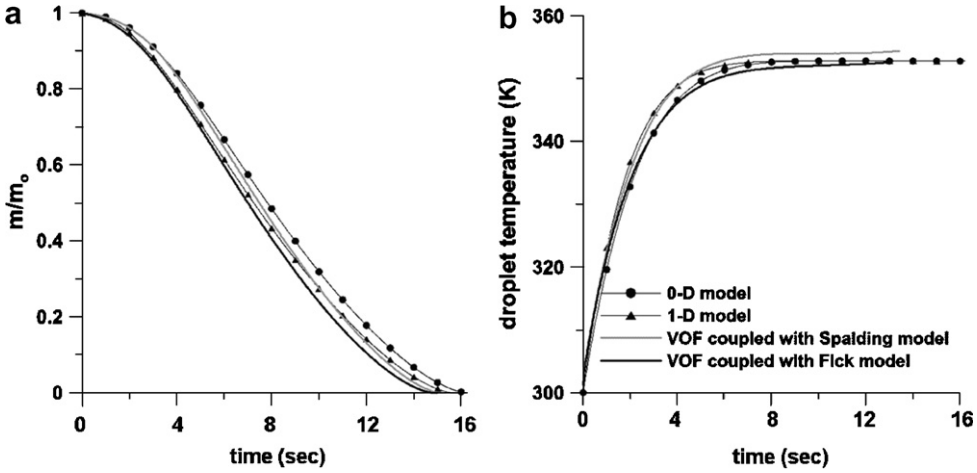

Fig. 2. Time evolution of (a) droplet mass and (b) mean temperature as calculated using various evaporation models.

In addition to that, the Spalding's finite conductivity model which takes into account the temperature distribution as function of the droplet radius [41,42] has been also used and referred to as the 1-D model. These models have been validated over a number of cases and they can be considered as accurate enough for the range of conditions relevant to this study. For the full liquid flow, heat transfer and vaporisation processes simulation that has to be validated, the above described VOF methodology has been coupled independently with both the Spalding's global evaporation model and the Fick's local evaporation model. Comparison of the results obtained with these four different approaches can be seen in Fig. 2. As it can be seen, the local evaporation model predicts accurately the evaporation process and it gives the same result as with all other three models. It has to be noted though that the Spalding's global evaporation model, can only be used in cases with a known reference length and certain flow conditions around the droplet (known in the present case), while Fick's local model, overcomes these limitations.

3.3. Boundary conditions

The computational domain is assumed to be axisymmetric, as shown in Fig. 3. The droplet's shape is initially approximated by a spherical cap sector. Two different grids are used in order to simulate the flow and temperature distribution of the surrounding gas, inside the liquid droplet, as well as the temperature distribution inside the solid wall.

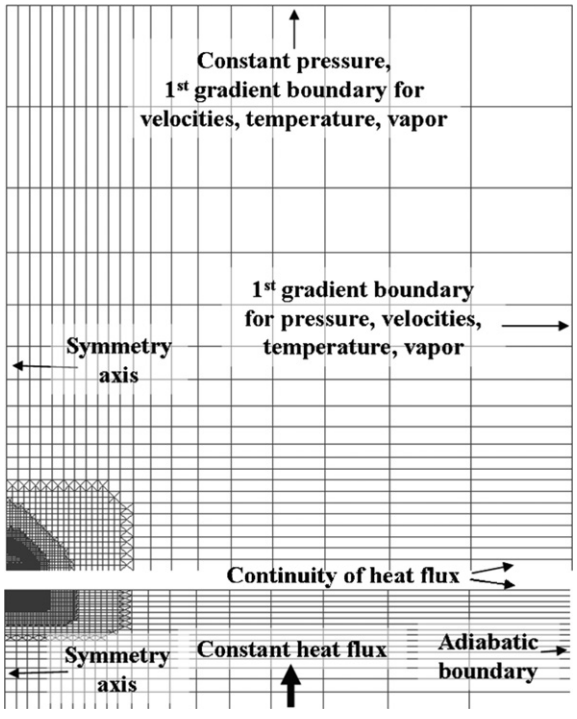

Fig. 3. Numerical grid and boundary conditions for the gas–liquid phase and the solid phase.

For the temperature and the vapour concentration field the following boundary conditions have been assumed; in the open boundaries for the case of velocity vectors facing inwards the computational domain, it has been assumed that the gas entering is dry air with 293 K temperature; for the case of velocity vectors facing outwards the computational domain, a zero 1st gradient boundary condition is assumed. A constant heat flux (different for each case) is assumed at the lower boundary of the solid and equal to the heat loss due to convection form the upper edge of the plate in order to keep the initial surface temperature constant. The initial temperature distribution inside the solid wall is assumed to be linear. An important part of the simulation is the coupling of the boundary conditions of the gas–liquid phase and the solid wall. Initially the wall has a constant temperature on its surface. During the solution it has been assumed that the heat fluxes between the common boundaries are equal, thus allowing estimation of the wall temperature at the common boundary cells. The contact angle changes during the evaporation process according to the total evaporation rate of the droplet. When the observed limit of receding contact angle is reached, the contact angle remains constant and the VOF methodology predicts then the reduction of the contact diameter.

3.4. Simplified model

The above described coupled liquid flow and heat transfer solution is computationally expensive, mainly due to the Courant number-based restrictions on the time step of the VOF methodology; typically, it requires more than 10 CPU days on a high-end single processor PC. As a result, it is not practical to be used for parametric studies of engineering interest. Therefore, a simplified model, similar to that proposed in [10] is also adopted here. This simplified model, which does not account for the fluid motion, speeds-up calculations about 30 times. The computational domain used in this approach is again assumed to be axisymmetric, as shown in Fig. 4a and b. Initially liquid vaporisation is calculated assuming that its contact area with the solid surface remains constant. The shape of the liquid is pre-defined and approximated with a spherical cap with decreasing height. This assumption holds until the contact angle at the air–liquid–solid interface reaches the experimentally determined receding contact angle. From that point onwards, the contact angle is assumed to remain constant; as a result vaporisation of the liquid retains a similarity of the droplet's shape and thus both liquid height and liquid–solid contact area decrease simultaneously until full vaporisation of the remaining liquid. The grid used was body-fitted in the liquid–solid system and remapping of the solved variables was performed at each time step.

The heat conduction equation is solved simultaneously inside the liquid and the solid material; the boundary conditions used are the following:

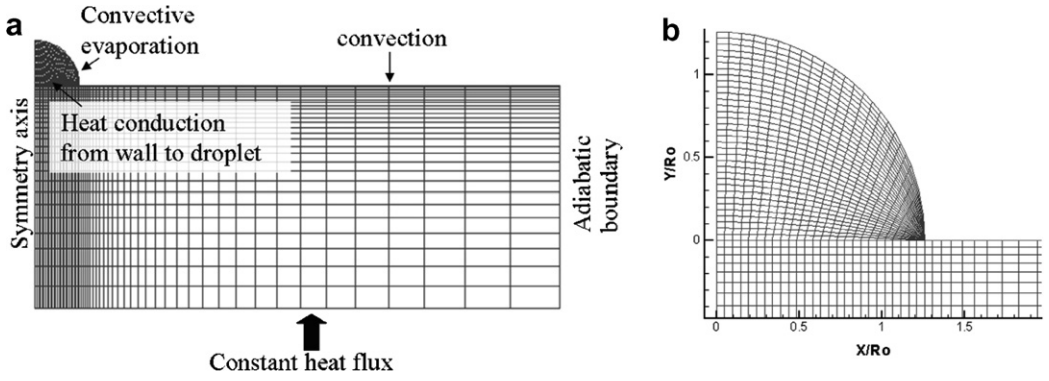

Fig. 4. (a) Numerical grid for the heat conduction calculation inside the liquid and the solid using pre-defined droplet shape and (b) detail of grid around the droplet area.

At the gas–liquid interface:

$$-k_{\mathrm{liq}}\frac{\mathrm{d}T}{\mathrm{d}n}=h_{\mathrm{conv-liq}}(T_{\mathrm{liq}}-T_{\infty})+\dot{m}_{\mathrm{evap}}L$$

At the gas–solid interface:

$$-k_{\mathrm{sol}}\frac{\mathrm{d}T}{\mathrm{d}n}=h_{\mathrm{conv-sol}}(T_{\mathrm{surf}}-T_{\infty}) \tag{12}$$

At the liquid–solid interface:

$$k_{\mathrm{liq}}\frac{\mathrm{d}T}{\mathrm{d}n}=k_{\mathrm{sol}}\frac{\mathrm{d}T}{\mathrm{d}n}$$

A constant heat flux is assumed at the lower boundary of the solution domain and equal to the heat loss due to convection form the upper edge of the plate, e.g. $q=h_{\mathrm{conv\text{-}sol}}\cdot(T_{\mathrm{surf}}-T_{\infty})$ in order to keep the surface temperature constant. The initial temperature distribution inside the liquid droplet is assumed to be uniform and equal to the mean value obtained at the end of the transitional period, as estimated by the VOF calculation. The initial temperature distribution inside the solid is assumed to be linear. The heat transfer coefficients are calculated from empirical correlations of the Nusselt number that can be found, for example in [43]. Modelling of the evaporation rate is rather critical, because a concentration equation for the vapour is not solved in the simplified model. Two evaporation models have been tested. The first one is the model of Spalding [41,42], which estimates the total evaporation rate for the whole droplet, as in Eq. (11). The second one is based on the kinetic theory of gases and it is usually referred to as the Hertz–Knudsen formula [27,44]. This model predicts the vaporisation rate locally at every point of the air–liquid interface. Integration around the droplet surface gives the total vaporisation rate of the droplet as

$$\frac{\mathrm{d}m}{\mathrm{d}t}=\lambda A_{\mathrm{drop}}\sqrt{\frac{Mw_{\mathrm{vap}}}{2\pi\Re}}\left(\frac{p_{\mathrm{s}}}{\sqrt{T_{\mathrm{s}}}}-\frac{p_{\infty}}{\sqrt{T_{\infty}}}\right) \tag{13}$$

The results of the application of the two models (original Hertz–Knudsen formula and Spalding's model) are compared in Fig. 5 for a typical case of a stagnant *n*-nonane droplet with diameter $D_0=7.4$ mm, initial droplet temperature $T_{\mathrm{dr0}}=400$ K at gas temperature $T_{\mathrm{gas0}}=400$ K. The two models predict a very different behaviour of the evaporation rate and droplet temperature. The kinetic theory model predicts a much lower evaporation rate at the late stages of evaporation (thus longer droplet life time) and an increase of the droplet temperature. A basic difference between the two models lies on the value of the mass transfer coefficient, which takes a constant value in the original kinetic theory model but variable one in the Spalding

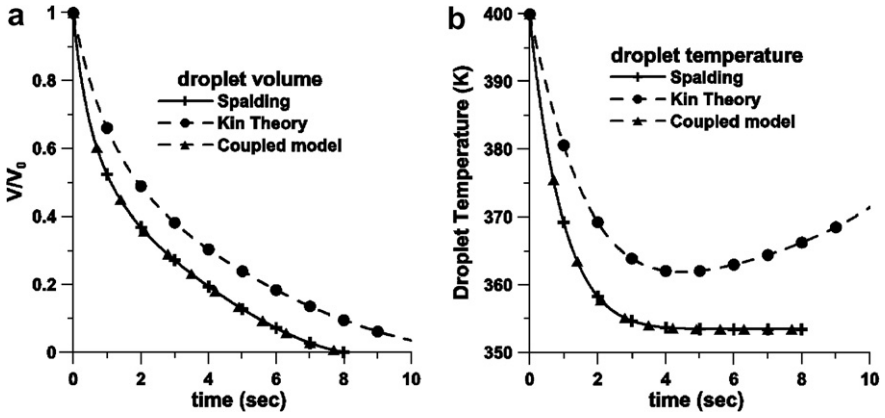

Fig. 5. Comparison between the Spalding's, the original kinetic theory model and the coupled model for the (a) droplet volume regression and (b) mean droplet temperature.

model. Since in principle the two models should predict the same vaporisation rate, an attempt is made here to relate the results obtained from these two models. This can be achieved by using the following formula for the accommodation coefficient λ:

$$\lambda = h_m \sqrt{\frac{2\pi M w_{vap}}{\Re T_s}} \frac{\ln(1+B_m)}{Y_s - Y_\infty \sqrt{T_\infty / T_s}} \tag{14}$$

It has been further assumed that the accommodation coefficient changes during the droplet evaporation, following the law:

$$\lambda = \lambda_0 \frac{h_m/\sqrt{T_s}}{h_{m0}/\sqrt{T_{s0}}} \times \frac{\ln(1+B_m)}{Y_s - Y_\infty \sqrt{T_\infty/T_s}} \left(\frac{Y_s - Y_\infty \sqrt{T_\infty/T_s}}{\ln(1+B_m)} \right)_0 \tag{15}$$

where the term h_{m0} is calculated from the initial conditions of the simulation with $Sh_0 = 2$ and λ_0 is the reference value of the accommodation coefficient. As it can be seen from the results also presented in Fig. 5, the two models are now predicting the same liquid volume reduction and mean liquid temperature during the evaporation process. For the case of a droplet in contact with a solid surface, a similar approach is used creating a coupled model relating the evaporation rate predicted from semi-empirical models to the locally determined evaporation rate of the kinetic theory. For this case, the evaporation rate is predicted by

$$\frac{dm}{dt} = \lambda A_{liq\text{-}cell} \sqrt{\frac{M w_{vap}}{2\pi \Re}} \left(\frac{p_s}{\sqrt{T_s}} - \frac{p_\infty}{\sqrt{T_\infty}} \right) \tag{16}$$

During the calculations, the properties of the solid material (stainless steel 304) were assumed constant. However, the properties of the liquid are assumed to be function of temperature [40] and thus they are updated at every calculation

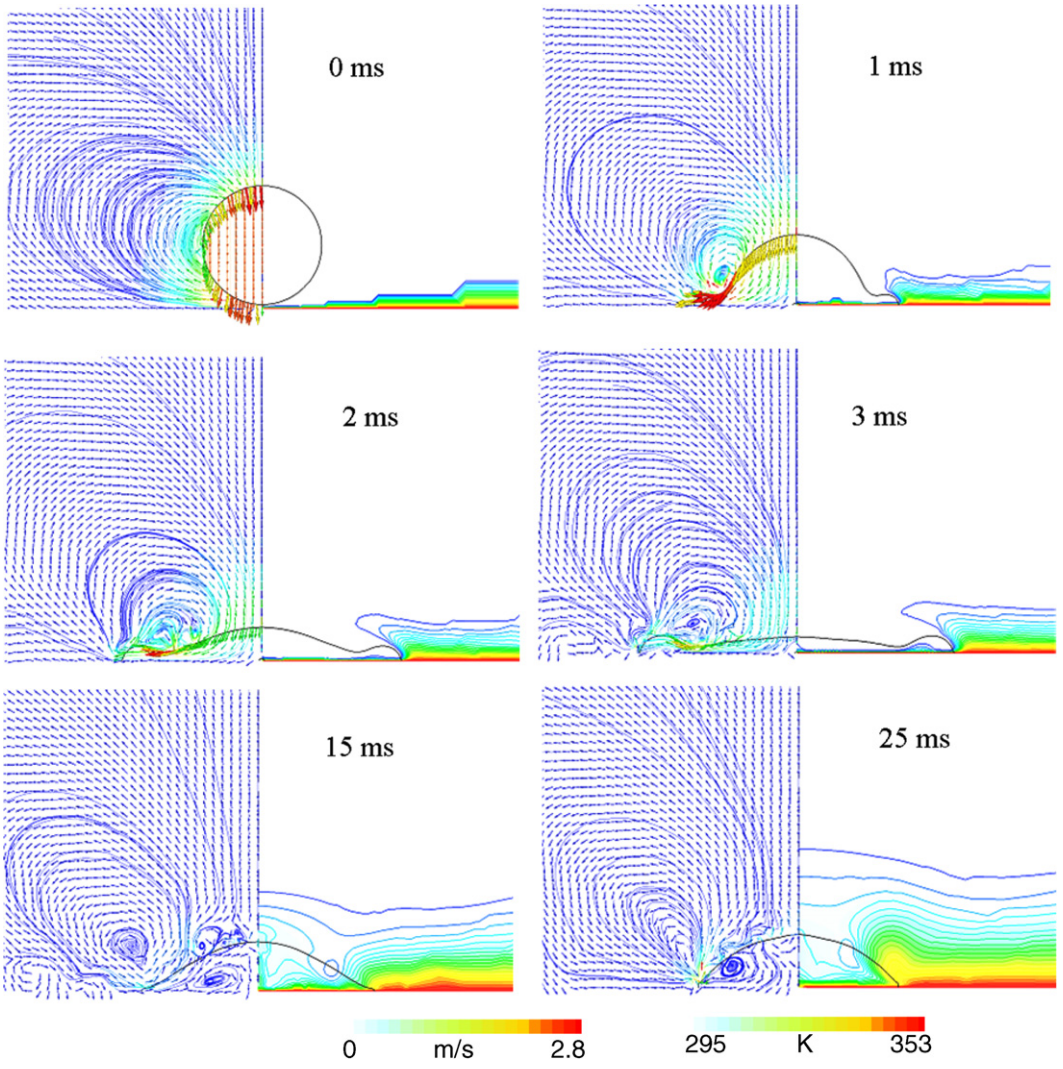

Fig. 6. Liquid droplet shape, streamlines, velocity vectors and temperature field as predicted by the VOF model during the transitional period from the droplet impingement until freezing of droplet motion is reached.

time step. The properties of the surrounding gas and vapour mixture are calculated using the 1/3 mixing rule.

4. Results and discussion

In this section the various results obtained with the computational models are presented and assessed against the experimental data of [10,33]. Initially, Fig. 6 is presented, showing representative frames of the temporal evolution of the temperature and velocity field during the transitional period of the droplet impact on the wall. The calculations have shown that the droplet temperature is not affected by the upper surface temperature, therefore, the transitional period is representative for all cases examined. Calculations have started at time $t = -0.05$ ms taking as reference of $t = 0$ is the time at which the droplet touches the wall. After the initial spreading following the droplet impact, which does not result to splashing, the liquid is forced by surface tension to return towards the centreline and take a spherical cup shape specified by the contact angle. The pressure and the vapour concentration fields as predicted by the VOF model are shown in Fig. 7 for the same time steps as the previous figure. Increased pressures are found at the point of impact and at the leading face of the droplet due to increased curvature of the free surface of the droplet, while a more uniform pressure distribution is found at the recoil phase. On the other hand, vapour concentration field reaches its maximum values at the leading edge of the droplet due to increased temperatures found in this area. The results confirm that under the given operating conditions, this process is not fast enough to result to droplet rebound; thus, the liquid rests and simply vaporises from that point onwards without any translational movement of its surface. The mass evaporated during the transitional period for all cases is less than 0.01% of the initial droplet mass. The predicted values are summarised in Table 1.

Table 1
Droplet mean temperature at the end of the transitional period and time for the droplet to reach a stable form for all test cases investigated

	$T_{surf0} = 333$ K		$T_{surf0} = 353$ K		$T_{surf0} = 373$ K	
$\theta_0 = 90°$ (ppm = 0)	307 K	28 ms	315 K	28 ms	323 K	30 ms
$\theta_0 = 55°$ (ppm = 100)	–		329 K	35 ms	–	
$\theta_0 = 20°$ (ppm = 1000)	–		340 K	34 ms	–	

Following the transitional period, the droplet stabilises on the surface and vaporises without any translational motion. The liquid and air motion is caused by free convection between the heated plate, the liquid and the surrounding air. Fig. 8 shows the predicted temperature distribution inside the liquid droplet and the wall for the case of 80 °C initial surface temperature and 90° initial contact angle. As can be seen, initially, the wall is cooled by the droplet which at the same time vaporises. Since heat is constantly added to the plate while the temperature of the droplet increases and its volume decreases, there is a point where the added heat becomes equal to the energy contacted to the droplet. Following that point, the wall temperature gradually starts to increase. Lower temperatures are found in the centre of the contact area, therefore, buoyancy effects within the droplet create internal recirculation region, which can be seen in Fig. 9. Two recirculation zones can

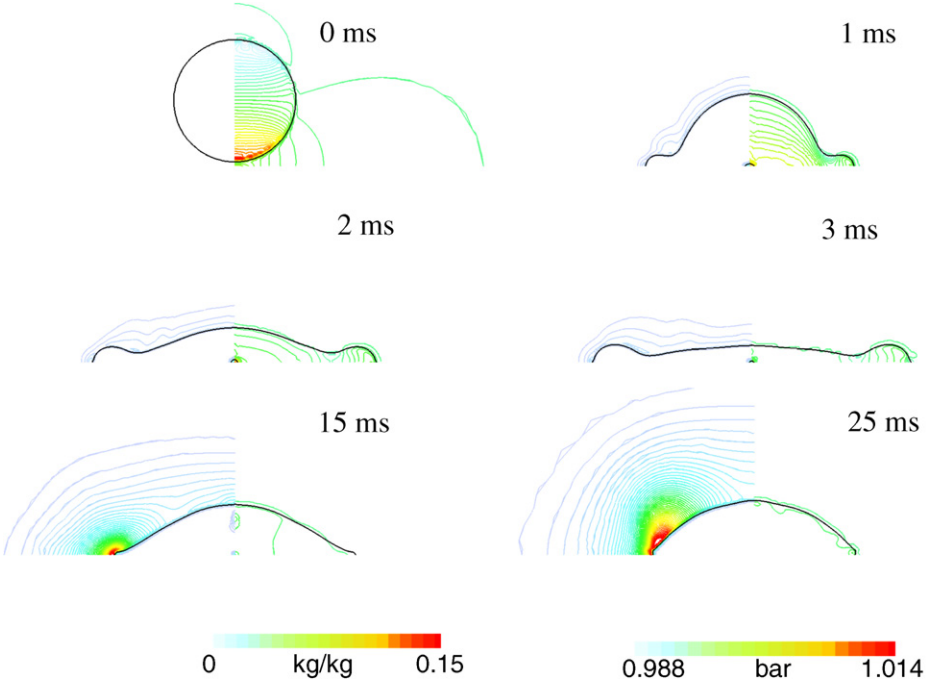

Fig. 7. Vapour concentration field and pressure field as predicted by the VOF model during the transitional period from the droplet impingement until freezing of droplet motion is reached.

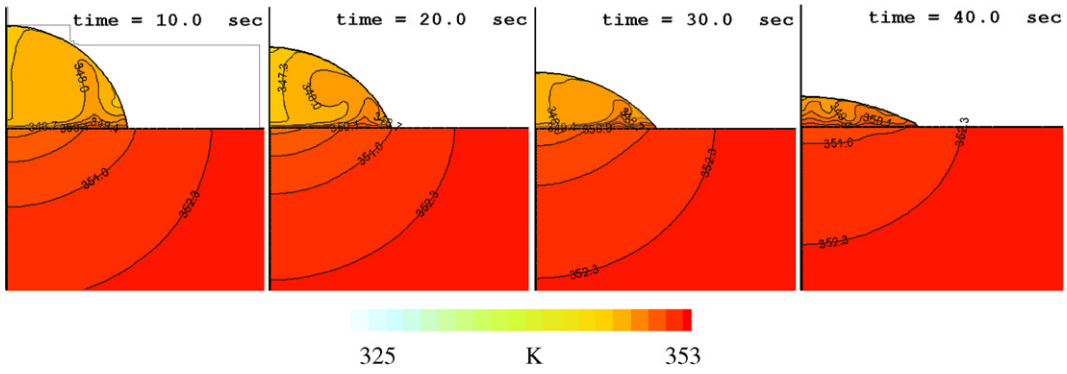

Fig. 8. Predicted temperature distribution within the liquid and the solid during the vaporisation process using the full solution (initial surface temperature 80 °C, initial contact angle 90°).

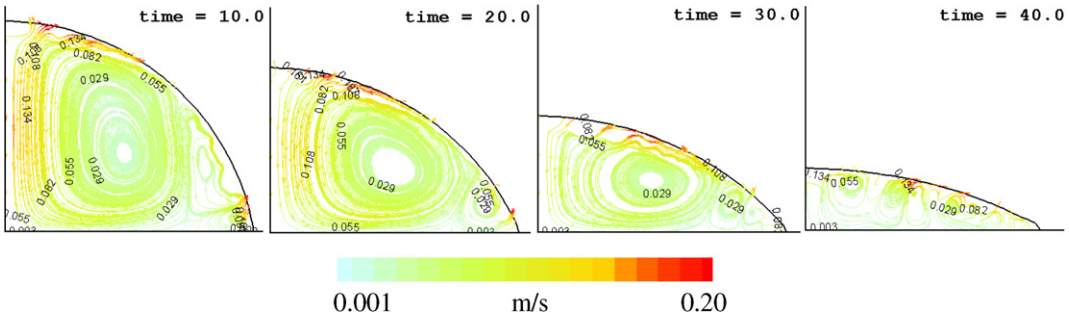

Fig. 9. Predicted streamlines within the liquid during the vaporisation process using the full solution (initial surface temperature 80 °C, initial contact angle 90°).

be observed. The bigger one occupies most of the droplet volume, while a smaller circulation is forming at the edge of the droplet, near the triple point of solid–liquid–gas. That recirculation enhances the local evaporation rate at this location, which takes its maximum value at this specific location. The distribution of the vaporisation rate per unit area on the droplet surface during the droplet vaporisation process can be seen in Fig. 10 for the case of 80 °C initial surface temperature and 90° initial contact angle. In order to compare the results of the full fluid flow and heat transfer simulation with the results of the simplified model where only the heat transfer is considered assuming a pre-described droplet shape as the droplet vaporises, Fig. 11 is presented for the same case. As can be seen by comparing the plotted temperature distribution with that of Fig. 8, temperature now follows an almost linear variation with the distance from the wall. As expected, the role of the induced flow motion is to mix the liquid faster compared to the heat conduction process and thus create a more uniform temperature field within the droplet. This is evident by the level of the contours plotted. At the same time, the actual cooling effectiveness of the liquid (i.e. the amount of heat contacted from the wall to the droplet) as predicted by the full and the simplified models, is different. Having in mind these differences between the two numerical solutions, we proceed now to the validation of the obtained results against the available experimental data.

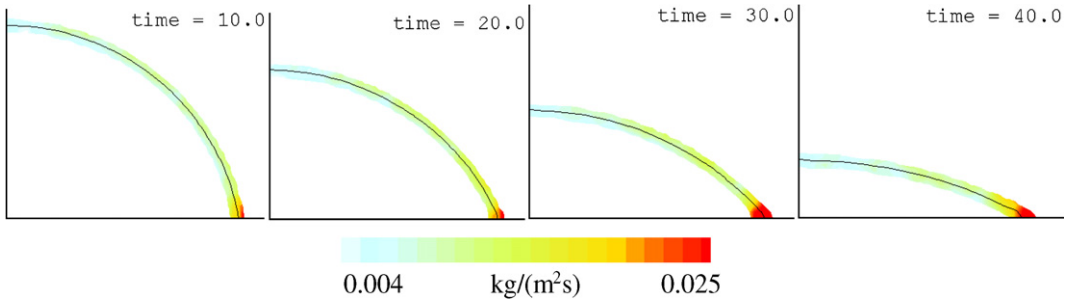

Fig. 10. Evaporation rate (kg/m^{2}s) on the liquid–gas interface, as predicted using the full solution (initial surface temperature 80 °C, initial contact angle 90°).

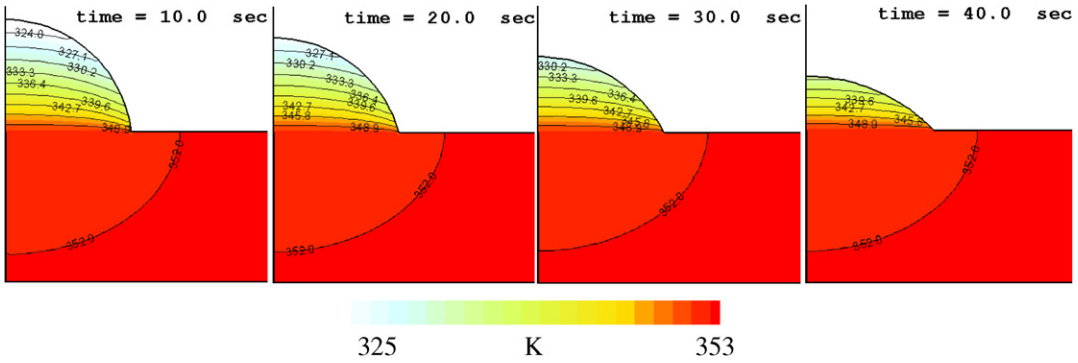

Fig. 11. Predicted temperature distribution within the liquid and the solid during the vaporisation process, as predicted by the simplified model (initial surface temperature 80 °C, initial contact angle 90°).

Fig. 12 presents the temporal evolution of droplet volume, liquid–solid contact angle and liquid–solid contact diameter as a function of initial contact angle, while Fig. 13 shows the same predictions but this time for different wall temperatures. In each graph, together with the experimental data of [10,33], three different sets of simulation results are presented. These refer to results obtained by the simplified model, by the full solution as well as from the full solution but this time assuming constant wall temperature. As can be seen, although the full solution approach and the simplified model are based on different principles and do result to different temperature distribution within the droplet, they predict similar evaporation behaviour and small differences in the total evaporation time. This is due to the effective application of the boundary condition in the gas–liquid interface of the simplified model (Eq.

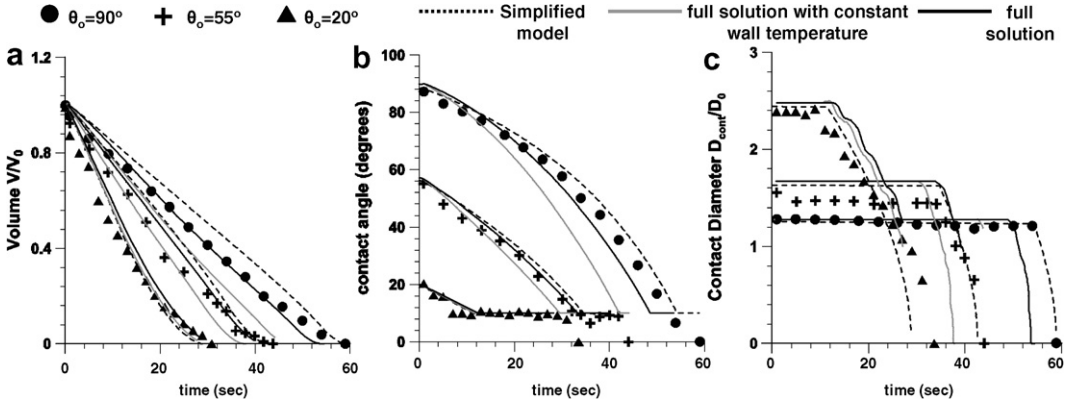

Fig. 12. Comparison between model predictions against the experimental data of [10,33], revealing the effect of contact angle on temporal evolution of (a) droplet volume, (b) solid–liquid contact diameter and (c) contact angle (initial surface temperature 80 °C).

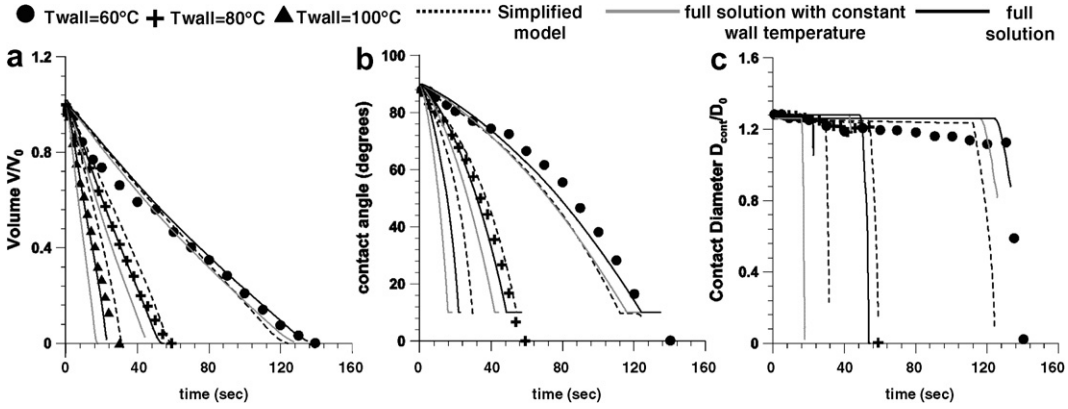

Fig. 13. Comparison between model predictions against the experimental data [10,33] revealing the effect of initial surface temperature on temporal evolution of (a) droplet volume, (b) solid–liquid contact diameter and (c) contact angle (initial contact angle 90°).

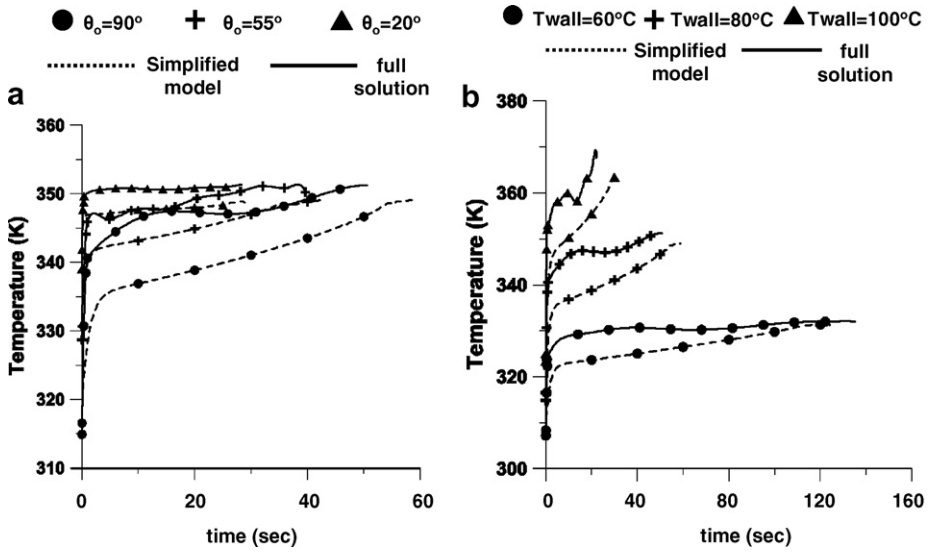

Fig. 14. Predicted temporal evolution of droplet's mean temperature using the different models tested for (a) different initial contact angles and (b) different initial wall temperatures.

(16)), which has been appropriately calibrated for one operating point and take into account the internal liquid motion effect and the vapour concentration gradient on the liquid–air interface. The full model, which does not require any ad-hoc calibration since it is based on the local (and variable around the droplet surface) vaporisation rate, gives the best predictions for all cases investigated. When the wall temperature variation is not considered, then the predicted vaporisation time is faster since the wall is kept at a higher temperature which enhances droplet heating, and thus vaporisation. In some cases, the predicted differences can be up to 20% compared with the experimental values. The calculated differences between the full and the simplified models are summarised in Fig. 14. This plot presents the temporal evolution of droplet mean temperature for all cases investigated up to full evaporation. Fig. 14a refers to the three cases of Fig. 12 where the initial contact angle varies while Fig. 14b refers to the cases of Fig. 13 where the initial wall temperature is modified. As can be seen, predictions from the full simulation model show a much faster rising of the droplet temperature compared to the simplified model. Thus, although the simplified model can provide reasonable vaporisation rates it requires appropriate calibration for a specific case, which makes it far from being applicable to other more complicated flow cases. The advantages of the full coupled heat transfer and fluid motion model where the vaporisation rate does not depend on the shape of the droplet–gas interface provides the most unrestrictive simulation approach to the problem.

An important application of the evaporation of a droplet in contact with a heated wall is the cooling of the substrate. A quantification of the cooling of the substrate can be obtained introducing the cooling effectiveness factor which compares the conduction through the wall with and without the droplet.

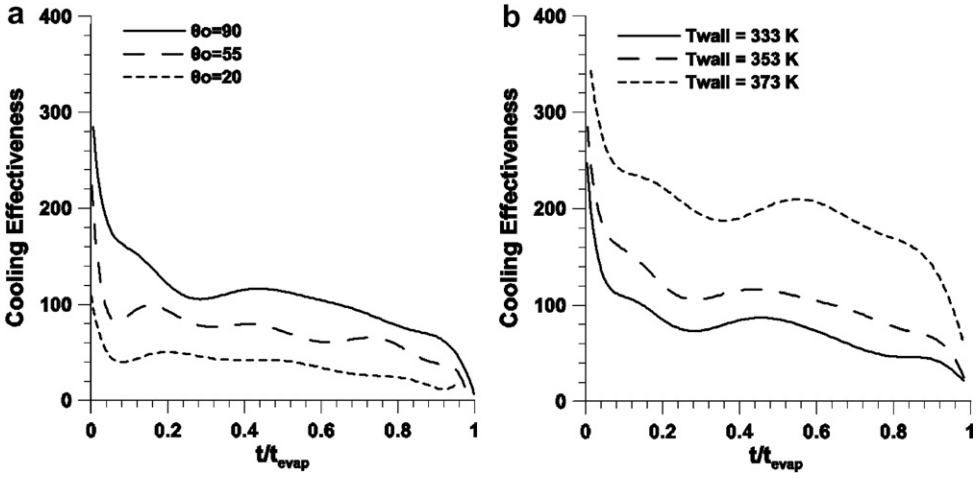

Fig. 15. Temporal evolution of the cooling effectiveness factor for (a) different initial contact angles and (b) different initial wall temperatures.

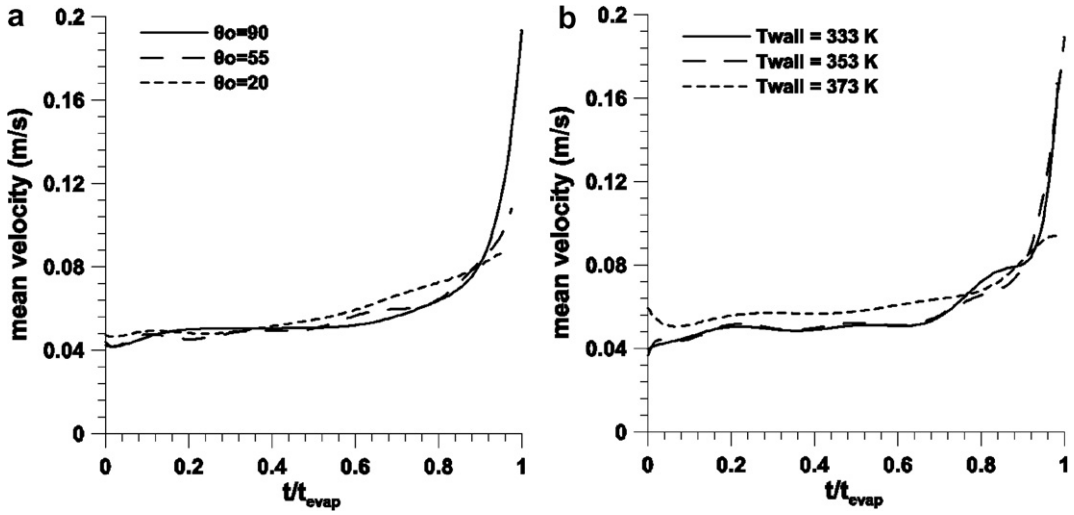

Fig. 16. Temporal evolution of the mean velocity inside the liquid phase for (a) different initial contact angles and (b) different initial wall temperatures.

$$\varepsilon = \frac{\left(\int_0^{D_{cont0}/2}\left(k\frac{dT}{dn}\right)r\,dr\right)_{with\_droplet}}{\left(\int_0^{D_{cont0}/2}\left(k\frac{dT}{dn}\right)r\,dr\right)_{without\_droplet}} - 1 \quad (17)$$

In Fig. 15 the temporal evolution of the cooling effectiveness factor is plotted. Time is non-dimensionalised with the total evaporation time for each case. As can be clearly seen, the cooling of the substrate is enhanced 50–250 times with an evaporating droplet in touch with it, while the cooling increases with increasing substrate temperature and contact angle. Finally, the model can provide insight on the strength of the flow motion induced within the droplet during the evaporation process. As already mentioned, inside the droplet a recirculation zone is formed due to buoyancy effects. In Fig. 16 the temporal evolution of the mean velocity of the liquid phase weighted with the cell volume is plotted for the different cases investigated. Noting that the droplet surface velocity at the end of the transitional period was found to be less than 0.02 m/s, it is clear that the liquid velocities induced by the heating and vaporisation within the liquid can be much greater. It is also noticeable that the strength of the recirculation zone increases substantially during the latest stages of the droplet life time.

5. Conclusions

The evaporation of droplets impinging and depositing on heated solid walls was studied numerically using a modified version of the VOF methodology able to account for heat transfer and surface vaporisation processes. The numerical methodology was coupled with an evaporation model predicting locally the variable droplet surface liquid vaporisation process. Appropriate boundary conditions were used for the solid–liquid–air contact angle while the heat conduction equation inside the solid phase was solved simultaneously with the flow equations. The heat transfer equation was solved both for the liquid phase and the solid wall using an adaptive grid technique. In addition to this model, a simplified numerical approximation was also employed, in which the internal flow circulation was neglected while the shape of the vaporising droplet was pre-described based on experimental observations; this approach reduces the calculation time up to 30 times compared to the full heat transfer and fluid flow simulation model. For this case, an improved evaporation model based on the Hertz–Knudsen formula and the Spalding evaporation model was formulated for the prediction of the evaporation rate of the droplet in contact with the hot wall. The numerical results have been compared against experimental data; these have included the temporal variation of the droplet volume, contact angle and liquid–solid contact diameter. The full model has been found to give the best predictions for all cases simulated, capturing not only the droplet volume change, which was also the case with the simplified model, but also the droplet shape evolution. The results have confirmed that the droplet lifetime decreases with increasing initial contact angle and surface temperature, while the local evaporation rate on the droplet surface takes its maximum value at the triple line of solid–liquid–gas interface. Finally, predictions obtained by assuming a fixed wall temperature and thus, neglecting the heat conduction inside the solid wall have resulted up to 20% faster vaporisation compared to the actual case.

Acknowledgement

This work has been partially supported by the Greek State Scholarships Foundation.

References

[1] L.H.J. Wachters, N.A. Westerling, The heat transfer from a hot wall to impinging water drops in the spheroidal state, Chem. Eng. Sci. 21 (1966) 1047–1056.

[2] T.Y. Xiong, M.C. Yuen, Evaporation of a liquid droplet on a hot plate, Int. J. Heat Mass Transfer 34 (7) (1991) 1881–1894.
[3] S. Chandra, C.T. Avedisian, On the collision of a droplet with a solid-surface, Proceedings of the Royal Society of London Series A – Mathematical Physical and Engineering Sciences 432 (1884) (1991) 13–41.
[4] S. Chandra, C.T. Avedisian, Observations of droplet impingement on a ceramic porous surface, Int. J. Heat Mass Transfer 35 (10) (1992) 2377–2388.
[5] K. Anders, N. Roth, A. Frohn, The velocity change of ethanol droplets during collision with a wall analyzed by image-processing, Exp. Fluids 15 (2) (1993) 91–96.
[6] Y.S. Ko, S.H. Chung, An experiment on the breakup of impinging droplets on a hot surface, Exp. Fluids 21 (2) (1996) 118–123.
[7] S.L. Manzello, J.C. Yang, On the collision dynamics of a water droplet containing an additive on a heated solid surface, Proc. R. Soc. London, Ser. A – Math. Phys. Eng. Sci. 458 (2026) (2002) 2417–2444.
[8] J.D. Bernardin, C.J. Stebbins, I. Mudawar, Effects of surface roughness on water droplet impact history and heat transfer regimes, Int. J. Heat Mass Transfer 40 (1) (1997) 73–88.
[9] J.D. Bernardin, I. Mudawar, C.B. Walsh, E.I. Franses, Contact angle temperature dependence for water droplets on practical aluminium surfaces, Int. J. Heat Mass Transfer 40 (5) (1997) 1017–1033.
[10] S. Chandra, M. diMarzo, Y.M. Qiao, P. Tartarini, Effect of liquid–solid contact angle on droplet evaporation, Fire Safety J. 27 (2) (1996) 141–158.
[11] H. Fujimoto, N. Hatta, Deformation and rebounding processes of a water droplet impinging on a flat surface above Leidenfrost temperature, J. Fluids Eng. – Trans. ASME 118 (1) (1996) 142–149.
[12] N. Hatta, H. Fujimoto, K. Kinoshita, H. Takuda, Experimental study of deformation mechanism of a water droplet impinging on hot metallic surfaces above the Leidenfrost temperature, J. Fluids Eng. – Trans. ASME 119 (3) (1997) 692–699.
[13] B.S. Gottfried, C.J. Lee, K.J. Bell, The Leidenfrost phenomenon: film boiling of liquid droplets on a flat plate, Int. J. Heat Mass Transfer 9 (1966) 1167–1187.
[14] L.H.J. Wachters, L. Smulders, J.R. Vermeulen, H.C. Kleiweg, The heat transfer from a hot wall to impinging mist droplets in the spheroidal state, Chem. Eng. Sci. 21 (1966) 1231–1238.
[15] A.K. Sen, C.K. Law, On a slowly evaporating droplet near a hot plate, Int. J. Heat Mass Transfer 27 (8) (1984) 1418–1421.
[16] T.K. Nguyen, C.T. Avedisian, Numerical-solution for film evaporation of a spherical liquid droplet on an isothermal and adiabatic surface, Int. J. Heat Mass Transfer 30 (7) (1987) 1497–1509.
[17] S. Zhang, G. Gogos, Film evaporation of a spherical droplet over a hot surface - fluid-mechanics and heat mass-transfer analysis, J. Fluid Mech. 222 (1991) 543–563.
[18] M. Pasandideh-Fard, R. Bhola, S. Chandra, J. Mostaghimi, Deposition of till droplets on a steel plate: simulations and experiments, Int. J. Heat Mass Transfer 41 (19) (1998) 2929–2945.
[19] M. Pasandideh-Fard, V. Pershin, S. Chandra, J. Mostaghimi, Splat shapes in a thermal spray coating process: simulations and experiments, J. Therm. Spray Technol. 11 (2) (2002) 206–217.
[20] M. Bussmann, J. Mostaghimi, S. Chandra, On a three-dimensional volume tracking model of droplet impact, Phys. Fluids 11 (6) (1999) 1406–1417.
[21] L.L. Zheng, H. Zhang, An adaptive level set method for moving-boundary problems: application to droplet spreading and solidification, Numer. Heat Transfer, Part B – Fundam. 37 (4) (2000) 437–454.
[22] R. Ghafouri-Azar, S. Shakeri, S. Chandra, J. Mostaghimi, Interactions between molten metal droplets impinging on a solid surface, Int. J. Heat Mass Transfer 46 (8) (2003) 1395–1407.
[23] Z. Zhao, D. Poulikakos, J. Fukai, Heat transfer and fluid dynamics during the collision of a liquid droplet on a substrate. 1. Modelling, Int. J. Heat Mass Transfer 39 (13) (1996) 2771–2789.
[24] Z. Zhao, D. Poulikakos, J. Fukai, Heat transfer and fluid dynamics during the collision of a liquid droplet on a substrate. 2. Experiments, Int. J. Heat Mass Transfer 39 (13) (1996) 2791–2802.
[25] J.M. Waldvogel, D. Poulikakos, Solidification phenomena in picoliter size solder droplet deposition on a composite substrate, Int. J. Heat Mass Transfer 40 (2) (1997) 295–309.
[26] V. Butty, D. Poulikakos, J. Giannakouros, Three-dimensional presolidification heat transfer and fluid dynamics in molten micro-droplet deposition, Int. J. Heat Fluid Flow 23 (3) (2002) 232–241.
[27] D.J.E. Harvie, D.F. Fletcher, A simple kinetic theory treatment of volatile liquid–gas interfaces, J. Heat Transfer – Trans. ASME 123 (3) (2001) 486–491.
[28] D.J.E. Harvie, D.F. Fletcher, A hydrodynamic and thermodynamic simulation of droplet impacts on hot surfaces, Part II: validation and applications, Int. J. Heat Mass Transfer 44 (14) (2001) 2643–2659.
[29] D.J.E. Harvie, D.F. Fletcher, A hydrodynamic and thermodynamic simulation of droplet impacts on hot surfaces, Part I: theoretical model, Int. J. Heat Mass Transfer 44 (14) (2001) 2633–2642.
[30] M. Dimarzo, D.D. Evans, Evaporation of a water droplet deposited on a hot high thermal-conductivity surface, J. Heat Transfer – Trans. ASME 111 (1) (1989) 210–213.
[31] S.S. Sadhal, M.S. Plesset, Effect of solid properties and contact-angle in dropwise condensation and evaporation, J. Heat Transfer – Trans. ASME 101 (1) (1979) 48–54.
[32] O.E. Ruiz, W.Z. Black, Evaporation of water droplets placed on a heated horizontal surface, J. Heat Transfer – Trans. ASME 124 (5) (2002) 854–863.
[33] Y.M. Qiao, S. Chandra, Experiments on adding a surfactant to water drops boiling on a hot surface, Proc. R. Soc. London, Ser. A – Math. Phys. Eng. Sci. 453 (1959) (1997) 673–689.
[34] N. Nikolopoulos, Numerical investigation of droplet flow during impingement, PhD Thesis, National Technical University of Athens, 2006.
[35] N. Nikolopoulos, A. Theodorakakos, G. Bergeles, Normal impingement of a droplet onto a wall film: a numerical investigation, Int. J. Heat Fluid Flow 26 (1) (2005) 119–132.
[36] C.W. Hirt, B.D. Nichols, Volume of fluid (VOF) method for the dynamics of free boundaries, J. Comput. Phys. 39 (1) (1981) 201–225.
[37] A. Theodorakakos, G. Bergeles, Simulation of sharp gas–liquid interface using VOF method and adaptive grid local refinement around the interface, Int. J. Numer. Methods Fluids 45 (4) (2004) 421–439.
[38] O. Ubbink, R.I. Issa, A method for capturing sharp fluid interfaces on arbitrary meshes, J. Comput. Phys. 153 (1) (1999) 26–50.
[39] H. Jasak, Error analysis and estimation for finite volume method with applications to fluid flows, PhD Thesis, Imperial College of Science Technology and Medicine, University of London, 1996.
[40] R.H. Perry, D.W. Green, Perry's Chemical Engineers' Handbook, seventh ed., McGraw-Hill, 1997.
[41] D.B. Spalding, The combustion of liquid fuels, in: Fourth Internatioanl Symposium on Combustion, The Combustion Institute, 1956.
[42] R.S. Miller, K. Harstad, J. Bellan, Evaluation of equilibrium and non-equilibrium evaporation models for many-droplet gas–liquid flow simulations, Int. J. Multiphase Flow 24 (6) (1998) 1025–1055.
[43] F.P. Incropera, D.P. de Witt, Fundamentals of Heat and Mass Transfer, third ed., Wiley, NY, 1990.
[44] P. Van Carey, Liquid–Vapour Phase-Change Phenomena, Taylor & Francis, 1992.